WOODS HOLE
OCEANOGRAPHIC
INSTITUTION

OAFlux High-Resolution Ocean-Surface Vector Wind Analysis Synergized from Satellite Scatterometers and Radiometers

Part II: Uncertainty Estimation

Lisan Yu and Xiangze Jin

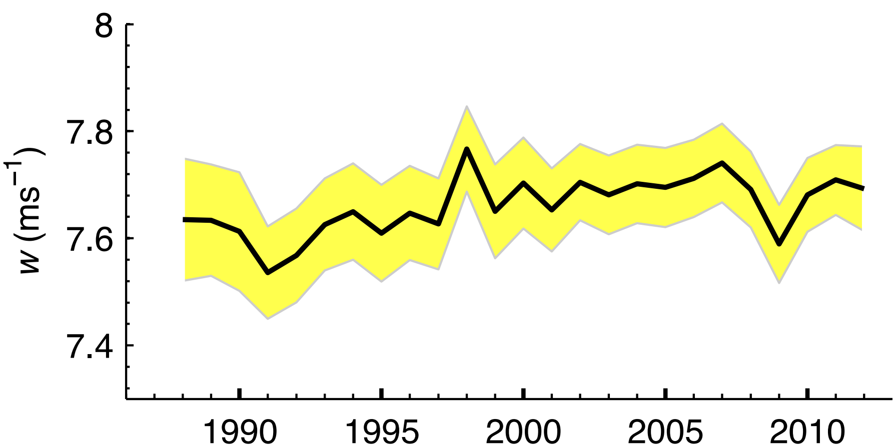

OAFlux Project Technical Report No. OA-2013-02
October 2013

Preface

A high-resolution global analysis of daily ocean-surface vector winds that covers the entire satellite wind observing period, from the first launch of SSMI in July 1987 to the present, was developed by the Objectively Analyzed air-sea Heat Fluxes (OAFlux) project. The OAFlux vector wind analysis is a synergy of 12 satellite sensors that includes 2 scatterometers (QuikSCAT and ASCAT) and 10 passive microwave radiometers (AMSRE, 6 SSMI sensors, and 2 SSMIS sensors, and the passive polarimetric microwave radiometer from WindSat).

A four-part report series is prepared, aiming to provide a systematic and conceptually organized review of the 12-sensor synergy and to support the public release of the datasets. Part I focuses on the methodology, approaches, and challenging technical issues in developing the multi-sensor synthesis. Part II documents the approach of error estimation that is developed to address the confidence and sensitivity of the OAFlux time series. Part III includes buoy-based validation. Part IV presents OAFlux time-mean fields of near-surface ocean vector winds and associated uncertainty estimates. The report series are developed from three research papers that were produced during the course of data development.

The datasets are freely available to interested users for non-commercial scientific research. For further information, please visit the project website at http://oaflux.whoi.edu/ or contact the project PI (lyu@whoi.edu). The project is sponsored by the NASA Ocean Vector Wind Science Team (OVWST) activities. We sincerely thank the NASA support and technical input given by the international OVWST community during the four-year development.

Project PI: Lisan Yu
Woods Hole Oceanographic Institution

Abstract

The high-resolution global daily analysis of ocean-surface vector winds from 1987 onward developed by the Objectively Analyzed air-sea Fluxes (OAFlux) project encompasses the entire era of satellite wind observations from scatterometers (wind speed and direction retrievals) and microwave passive radiometers (wind speed retrievals). This 25-year time series shows a distinct decadal upward trend and rich variability on broad timescales. Yet, significance of the trend and variability can be assessed confidently only when error statistics of the time series are known. Wind retrievals have large uncertainties under rain and high winds (>15ms^{-1}), due to technical difficulties inherent to both scatterometers and radiometers alike. The confidence and sensitivity of the OAFlux time series to uncertainties in satellite retrievals are addressed in this study.

The OAFlux approach is a weighted objective analysis, with the weights inversely proportional to errors in input datasets. An approach was then developed to rely on an ensemble of weight-perturbed analyses to compute the statistical expectations of the objective analysis. It is found that ~2% of global daily wind fields are subject to rain and high winds that are primarily associated with the tropical rain belts and the mid-latitude storms. When averaged globally and over the 25-year period, the mean standard deviation (STD) error is estimated to be 0.21 ms^{-1} in wind speed, 0.30 ms^{-1} and 0.32 ms^{-1} in zonal and meridional winds, respectively. Given the error estimates, the decadal upward trend in the time series is significant at the 95% confidence level.

This is the second part of the four-part technical report series and was developed from the research paper entitled “A satellite-derived high-resolution ocean-surface vector wind analysis (1987 onward). Part II: Confidence and sensitivity to rain and high winds”.

Key words: remote sensing of ocean surface winds, scatterometer, passive microwave radiometer, high winds, climate change and variability

Table of Contents

1. Introduction and Background

The Objectively Analyzed air-sea Heat Fluxes (OAFlux) project at the Woods Hole Oceanographic Institution (WHOI) is a research project, with central foci on air-sea exchanges of heat, moisture, and momentum and their role in global climate variability and change. The OAFlux has distributed global time series of ocean evaporation, air-sea latent and sensible heat fluxes, and flux-related surface meteorological variables from 1958 onward with a near real-time update (http://oaflux.whoi.edu). In the past four years, efforts have been devoted to develop a high-resolution (0.25-degree) global daily analysis of ocean-surface vector winds for the satellite period (July 1987 onwards) through synergizing 12 sensors including both scatterometers and passive microwave radiometers. The new 25-year analysis of ocean surface vector wind extends OAFlux existing surface flux data base, making it a site of choice for consistent, quality, multidecadal time series of air-sea heat, moisture, and momentum fluxes.

The technical report series have four parts, aiming to provide a systematic and conceptually organized review of the 12-sensor synergy and to support the public release of the datasets. The first part addresses the methodology, approaches, and challenging technical issues in developing the multi-sensor synthesis is detailed in Part I [*Yu and Jin* 2013a]. This second part focuses on the approach of error estimation that is developed to address sensitivity of the OAFlux time series to intersensor differences at high winds and heavy rainfall conditions and to quantify the confidence of the synthesis. The report provides an extended description of the methodology on error estimation, with major results drawn from a research paper, entitled "A satellite-derived high-resolution ocean-surface vector wind analysis (1987 onwards). Part II: Confidence and sensitivity to rain and high winds" [*Yu and Jin* 2013b].

The OAFlux wind analysis is a synergy of 12 satellite sensors, including 2 scatterometers (QuikSCAT and ASCAT) that have wind speed and direction retrievals, and 10 passive microwave radiometers (6 SSMI sensors - F08, F10, F11, F13, F14, and F15; 2 SSMIS sensors – F16 and F17, AMSR-E, and the passive polarimetric microwave radiometer from WindSat) that have wind speed retrievals. This 25-year time series encompasses the entire era of satellite wind observations from 1987 onward and shows a distinct decadal upward trend and rich variability on broad timescales [*Yu and Jin* 2012; 2013a]. Yet, the significance of the trend and variability in a time series can be assessed confidently only when error statistics of the time series are known. This second part of the study focuses on the confidence and sensitivity of the OAFlux time series to uncertainties in satellite retrievals.

Providing an uncertainty analysis to a dataset that is constructed from multiple satellite sensors is not straightforward, since input satellite retrievals products usually do not have error estimates. There are several studies in literature on analyzing errors in the gridded products that include both random measurement errors and representation errors (or biases) [e.g., *Stoffelen* 1998; *Schlax et al.* 2001; *Milliff et al.* 2004; *Kent and Challenor* 2006; *Kent and Kaplan* 2006; *Bourassa and Ford* 2010; *Vogelzang et al.,* 2011; *Bentamy et al.* 2012], with some offering practical approach on estimating the total error contribution. For instance, the Global Precipitation Climatological Project (GPCP) constructed error estimates from the dispersion (or spread) of eight different ocean precipitation products in reference to GPCP [*Adler et al.* 2012]. The SST 0.25-degree analysis by *Reynolds et al.* [2007] is based on optimal interpolation that requires the specification of the correlations and variances, for which in situ SST observations were introduced to determine the statistics of correlations through a least-squares fitting [*Smith and Reynolds* 2004].

We present in this study an innovative approach for assessing the confidence and uncertainty of the 12-sensor synthesized OAFlux wind analysis. The approach was developed from the relation of the objective formulation to the errors in the input datasets. The methodology of the OAFlux synthesis is based upon the least-variance linear statistical estimation [*Lorenc* 1988; *Daley* 1991; *Talagrand* 1997], which requires the formulation of the least-squares estimator (the so-called cost function) to include both data constraints and kinematic constraints (e.g., vorticity and divergence). Error information is needed for computing the weight associated with each constraint to determine the contribution of the constraint to the solution. In this sense, the optimality of the solution is dependent of the weights (or data errors). Yet, in most practices the weights have to be assigned due to the lack of the error information on the input datasets, and such assignments would naturally introduce a degree of uncertainty to the solution of the objective analysis. The questions thus raised are, what are possible error sources of the input datasets? What is the relationship between the errors in input datasets and the uncertainty of the solution? And how to quantify the uncertainty of the solution? The OAFlux uncertainty analysis was established during the process of finding answer to these questions.

Yu and Jin [2013a] reported that the most challenging situation for the OAFlux 12-sensor synthesis is the construction of the near-surface circulation associated with synoptic weather storms that feature both high winds (>15 ms^{-1}) and rain conditions. Three factors contribute to the challenge. The first is the lack of microwave radiometer retrievals when it rains. The primary channel that radiometers use to retrieve wind is the 37 GHz channel [*Wentz* 1997], which is higher than scatterometers (e.g., QuikSCAT at 13.4 GHz and ASCAT at 5.255 GHz). The longer the wavelength is, the more sensitive the sensor is to the impacts of rain. Retrieving the surface wind in rain conditions by radiometers is thus inhibited. The second factor is the contamination of QuikSCAT wind vector cells (WVCs) by rain. Rain affects scatterometer retrievals by inducing a positive bias at low wind speeds (due to signal backscatter by rain drops) and a negative bias at high wind speeds (due to the atmospheric attenuation of signal). The wind direction is less affected by rain, except at high rain rates [*Quilfen et al.* 1998; *Yueh et al.* 2001; *Weissman et al.* 2002b]. QuikSCAT retrievals are most sensitive to heavy rain (above 8 mm/hr) and hence, the rain-flagged QuikSCAT WVCs need to be eliminated before using QuikSCAT in applications [*Stiles et al.* 2002; *Dunbar et al*. 2006; *Ricciardulli and Wentz*, 2011; *Fangohr* and *Kent*, 2012]. The elimination of rain leaves data voids, which cannot be easily filled in by the background dataset (e.g. the atmospheric reanalysis such as the ERAinterim) due to the differences between satellite and model fields. The third factor is the scatterometer difference at high wind conditions in rain free conditions. ASCAT high winds are found to be persistently lower than QuikSCAT high winds [e.g. *Soisuvarn et al.* 2008; *Vogelzang et al.* 2011; *Bentamy et al.* 2012; *Portabella et al. 2012*]. *Yu and Jin* [2013, JGR, submitted] showed that ASCAT is about 5 ms^{-1} lower when QuikSCAT wind speed is at 20 ms^{-1}, and about 8 ms^{-1} lower when the latter is at 30 ms^{-1}. They also showed that two experiments that were conducted in assessing the respective influence of ASCAT and QuikSCAT on the synthesis showed that the large-scale pattern and magnitude are barely affected by the inter-scatterometer differences but the surface wind fields associated with synoptic weather systems are scatterometer-dependent.

However, high winds constitute a mere 2% of the global ocean surface wind fields, while low winds (<5 ms^{-1}) and moderate winds (5–15 ms^{-1}) constitute the respective 20% and 78%. Under rain-free conditions, the 12 sensors included in OAFlux possess a high degree of agreement with each other and with buoy wind measurements when wind speeds are in the low-to-moderate wind speed range [*Yu and Jin* 2012], but they start to differ when wind speeds are 15 ms^{-1} and higher. The inter-sensor differences at high winds are explainable from the technical viewpoint of the sensors. Scatterometers measure the backscatter response at the sea surface, while microwave radiometrers measure the emissivity of the sea surface. Scattering and emission from the sea surface both describe the electromagnetic wave diffraction from surface short-scale waves that generate surface roughness in the vicinity of the Bragg resonance. The two sensors have a similar angular dependence of short waves on the ocean surface, but differ in their dependence on the incidence angle with respect to the longer wave tilting effect, particularly at high wind speeds (>15ms^{-1}) [*Donelan and Pierson* 1987; *Plant et al.* 1999; *Yueh et al.* 1997; *Weissman et al.,* 2002a; *Freilich and Vanhoff* 2003].

The statistically-based objective approaches, such as the one used by OAFlux, are not expected to mitigate the impacts of satellite technical difficulties during the synergy of sensors from multi platforms. These approaches are capable of reducing random errors (noises) within given retrievals and producing an optimal estimate that has a minimum variance. They are, however, unable to generate an improved estimate in the presence of missing or biased retrievals. Given that nearly 98% of global ocean surface wind fields can be constructed with confidence from high-quality satellite wind retrievals and the remaining 2% are affected by technical issues inherent to satellite scatterometers and radiometers, the focus of the assessment of the uncertainty of the OAFlux wind analysis will be on the wind estimates associated with rain and high wind conditions. Therefore, two specific objectives are pursued here. One is to develop the uncertainty estimation approach by utilizing the sensitivity of the objective analysis to the weights (section 2), and the other is to use the computed error estimates to characterize and define the confidence of the analysis in rain and high wind conditions (section 3). Summary and discussion are included in section 4.

2. Methodology and formulation of uncertainty analysis

2.1 Uncertainty analysis for wind speed and components

The variational formalism that establishes the OAFlux weighted objective synthesis is based upon the theory of least-variance linear statistical estimation [*Lorenc* 1988; *Daley* 1991; *Talagrand* 1997]. This approach has been commonly used in removing directional ambiguity during processing satellite scatterometer retrievals [*Hoffman* 1984; *Stoffelen and Anderson* 1997], in constructing gridded vector wind climatology from ship-based observations [*Legler et al.* 1989], and in developing ocean surface wind vector analysis from Cross-Calibrated Multi-Platform (CCMP) sensors [*Hoffman et al.* 2003; *Atlas et al.,* 2011]. The cost function formulated for the OAFlux multi-sensor synthesis is expressed as follows:

$$F = \underbrace{\frac{1}{2}(\vec{V}_a - \vec{V}_b)^T R_b(\vec{V}_a - \vec{V}_b)}_{\text{(I)}} + \underbrace{\frac{1}{2}(\vec{V}_a - \vec{V}_o)^T R_o(\vec{V}_a - \vec{V}_o)}_{\text{(II)}} + \underbrace{\frac{1}{2}(w_a - w_o)^T S_o(w_a - w_o)}_{\text{(III)}} + \cdots$$
$$+ \underbrace{\gamma(\nabla\times\vec{V}_a - \nabla\times\vec{V}_b)^2}_{\text{(IV)}} + \underbrace{\lambda(\nabla\cdot\vec{V}_a - \nabla\cdot\vec{V}_b)^2}_{\text{(V)}} \qquad (1)$$

where $\vec{V} = (u, v)$ is wind vector with zonal and meridional wind components denoted as u and v, respectively, and $w = \sqrt{u^2 + v^2}$ is wind speed. The superscript "T" denotes transpose. There are three subscripts: "a" denotes an estimate, "b" the background information, and "o" satellite observations. Two atmospheric surface wind reanalyses are used as the background data, including the European Centre for Medium-Range Weather Forecasts Re-Analysis (ERA) interim project and the Climate Forecast System Reanalysis (CFSR) from the National Centers for Environmental Prediction (NCEP). There are 12 satellite sensors, including SSMI F08, F10, F11, F13, F15, SSMIS F16, F17, AMSRE, WindSat, QuikSCAT, and ASCAT. Note that among the 12 sensors, QuikSCAT and ASCAT have observations of zonal and meridional wind components while all others are radiometers providing only wind speed observations. WindSat is used as a radiometer in the OAFlux synthesis, since its wind direction retrievals have large uncertainty when compared to buoy measurements and with QuikSCAT [*Yu and Jin* 2012]. The matrices R_b, R_o, and S_o are weighting matrices that, theoretically, are inversely proportional to the respective error covariance matrices of the background wind vector fields ($\vec{V_b}$), satellite wind vector observations ($\vec{V_o}$), and satellite wind speed observations (w_o). However, none of input data sources provide error statistics, and these weight matrices need to be specified using a priori information. For the OAFlux synthesis, the specification was based on buoy wind time series measurements at more than 120 sites [*Yu and Jin* 2012]. Readers are referred to *Yu and Jin* [2013a] for a description of satellite sensors, download data sources, and the synthesis procedure.

There are five terms in the cost function (1). The first three terms (I)-(III) are data constraints that represent a least-square fitting of the analyzed zonal wind, meridional wind, and wind speed to input background and satellite data sets. ERAinterim and CFSR supply the background information that is needed for two occasions: (i) initialization of wind direction when there are no scatterometer measurements prior to 1999, and (ii) gap-filling missing values in satellite observations. The fourth and fifth terms (IV)-(V) are weak constraints based on vorticity and divergence of ERAinterim and CFSR, and the contribution of these kinematic terms to the minimization process is set to be small by prescribing the scaling γ and λ respectively.

The minimization process seeks an optimal estimate of daily wind field that satisfies the data constraints (i.e., terms (I)-(III) in Eq.(1)) within the specified weight matrices for the given sets of weak constraints (i.e., terms (IV)-(V)). Although significant efforts have been made in using 120+ buoys to evaluate error statistics of input satellite and reanalyses datasets in an effort to provide the best possible values for weights R_b, R_o, S_o, the global representation of the weight assignments is unknown, particularly in conditions of high winds/heavy rain where buoy measurements are lacking and satellite retrievals deviate from each other. According to the theorem of the least-square fitting, uncertainty in optimal solution is related to the dispersion of input data. The larger the spread is, the larger the uncertainty will be, and vice versa. If the weights are not known exactly and have to be assigned, then the optimal solution obtained from the minimization process may not be unique – in a sense that the solution changes with the change of weight assignments. Hence, there will be N sets of optimal solutions when N sets of weight assignments are given. This establishes the central concept of our uncertainty analysis: uncertainty of the estimation can be calculated from the N sets of optimal solutions obtained from the N sets of sensitivity experiments that test weight assignments.

For simplicity, we assume that the weights are constant and the cost function for the OAFlux wind analysis (1) can be simplified as follows:

$$F = \frac{1}{2}\sum_{i=1}^{I} \alpha_i \,(u_a - u_i)^2 + \frac{1}{2}\sum_{i=1}^{I} \alpha_i \,(v_a - v_i)^2 + \frac{1}{2}\sum_{j=1}^{J} \beta_j \,(w_a - w_i)^2 + \text{weak constraints} \tag{2}$$

where α_i represents the weight assignment for zonal and meridional wind components, with the subscript $i = 1, \ldots, I$ indicating the respective input satellite (i.e., QuikSCAT and ASCAT) plus background (i.e., ERAinterim and CFSR) data sets for wind components. The weight assignment for the wind speed term is denoted by β_j, with the subscript $j = 1, \ldots, J$ indicating the respective input satellite wind speed data sets (e.g., SSMI F08, F10, F11, F13, F15, SSMIS F16, F17, AMSRE, WindSat, QuikSCAT, and ASCAT). In choosing the weights for the sensitivity experiments, the following relationship is used:

$$\textstyle\sum_{i=1}^{I} \alpha_i + \sum_{j=1}^{J} \beta_j = 1 \tag{3}$$

The contribution of the weak constraints (i.e., terms (IV) and (V)) is small and can be neglected in formulating the uncertainty estimation. By doing so, the analytic solution for w_a, u_a and v_a that minimizes F can be expressed as follows:

$$w_a = \textstyle\sum_{j=1}^{J} \beta_j \, w_j + \sqrt{(\sum_{i=1}^{I} \alpha_i \, u_i)^2 + (\sum_{i=1}^{I} \alpha_i \, v_i)^2} \tag{4}$$

$$u_a = \textstyle\sum_{i=1}^{I} \alpha_i \, u_i \Big/ \left(1 - \frac{1}{w_a} \sum_{j=1}^{J} \beta_j \, w_j\right) \tag{5}$$

$$v_a = \textstyle\sum_{i=1}^{I} \alpha_i \, v_i \Big/ \left(1 - \frac{1}{w_a} \sum_{j=1}^{J} \beta_j \, w_j\right) \tag{6}$$

The dependence of w_a, u_a and v_a on input data sets w_i, u_i and v_j, as well as on weights α_i and β_j, is seen in Eqs. (4)-(6). When the N sets of weight assignments are tested, the resulting N sets of the solution for w_a, u_a and v_a can be used to determine the uncertainty of the solution. We follow the common practice and compute the uncertainty from the dispersion of the N sets of the solution using the standard deviation (STD). Therefore, the uncertainty of w_a, u_a and v_a can be written as

$$\sigma_W = STD(w_{a,n}) \tag{7a}$$

$$\sigma_u = STD(u_{a,n}) \tag{7b}$$

$$\sigma_v = STD(v_{a,n}) \tag{7c}$$

where $n = 1, \ldots N$, denoting the N sets of the solution corresponding to N sets of weight assignments. In the OAFlux analysis, the weights were determined from the buoy-based evaluation on each input dataset [*Yu and Jin 2012*]. Here, the weights are randomly generated with one constraint applied, that is, the sum of all the weights is equal to one (see Eq. (3)). A total of 40 sets of weights was applied to Eqs. (4)-(6) in calculating Eqs. (7a-c). Further increase of the number of weight sensitivity experiments does not change the statistics, because the degree of freedom for errors is determined by the number of input datasets and not the number of sensitivity experiments.

Errors in the gridded products include both random errors and representation errors (or biases) [*Daly* 1993]. Random errors are the errors due to measurement noises, and can be reduced to near zero by significant spatial and temporal averaging. Representation errors are the errors due to unsolved scales or processes, and cannot be reduced by averaging. The methodology used here (Eqs. 7a-c) is, in essence, to reply on an ensemble of perturbed analyses [*Talagrand* 1997; *Desroziers et al.* 2009] to compute the expectations of the cost function from a set of randomly chosen weights. One expects that such an ensemble-based posteriori diagnostics would cancel out the random errors, yielding an error field that is dominated by representation errors.

2.2 Uncertainty analysis for wind stress and components

The focus of this study is on error estimation of wind speed and components, as they are the independent variables determined from the OAFlus synthesis. Nevertheless, errors of wind stress can be readily derived once errors of wind are known, because of the functional relationship between the two. This is demonstrated as follows. The wind stress, τ, and zonal and meridional stress components, τ_x and τ_y, are computed from the bulk formula [*Fairall et al.*, 2003]:

$$\tau = \rho C_d w^2 \tag{8a}$$

$$\tau_x = \rho C_d w u \tag{8b}$$

$$\tau_y = \rho C_d w v \tag{8c}$$

where ρ is the density of air, C_d drag coefficient. Given the relationship between τ and w in Eqs. 8a-c, the uncertainty estimation for wind stress and components is a problem of uncertainty propagation. Specifically, the uncertainty of τ is related to the uncertainty of w in the following way:

$$\sigma_\tau = \sqrt{\sigma_w^2 \left(\frac{\partial \tau}{\partial w}\right)^2} = \frac{2\tau}{w}\sigma_w \tag{9}$$

Accordingly, the uncertainty of τ_x, denoted σ_{τ_x}, can be derived from the uncertainty of u as follows:

$$\sigma_{\tau_x} = \sqrt{\sigma_u^2 \left(\frac{\partial \tau_x}{\partial u}\right)^2 + \sigma_v^2 \left(\frac{\partial \tau_x}{\partial v}\right)^2 + 2\sigma_{uv}\left(\frac{\partial \tau_x}{\partial u}\right)\left(\frac{\partial \tau_x}{\partial v}\right)} \tag{10}$$

The assumption that the correlation between τ_x and τ_y is negligible further simplifies Eq.(10) to the following form:

$$\sigma_{\tau_x} \approx \sqrt{\sigma_u^2 \left(\tau_x \left(\frac{1}{u} + \frac{u}{w^2}\right)\right)^2 + \sigma_v^2 \left(\tau_x \frac{v}{w^2}\right)^2} \tag{11}$$

Similarly, the uncertainty of τ_y, denoted σ_{τ_y}, can be expressed as

$$\sigma_{\tau_y} \approx \sqrt{\sigma_u^2 \left(\frac{\partial \tau_y}{\partial u}\right)^2 + \sigma_v^2 \left(\frac{\partial \tau_y}{\partial v}\right)^2} = \sqrt{\sigma_v^2 \left(\tau_y \left(\frac{1}{v} + \frac{v}{w^2}\right)\right)^2 + \sigma_u^2 \left(\tau_y \frac{u}{w^2}\right)^2} \qquad (12)$$

For the special case such as u = 0, Eq.(11) is the same as Eq.(9) because *w=abs(v)*. Likewise, Eq.(12) is identical to Eq.(9) if *v=0*. Structure of mean error fields computed from Eqs. (9), (11), and (12) can be found in the Technical Report Part IV and are not discussed here, as the analysis bears similarity to that of error fields of *w, u*, and *v*.

3. Results and analysis

3.1 Error characteristics in mean fields

The errors in the following discussions refer to the STD of *w, u, v* with respect to different sets of weight assignments (Eqs. 7a-c), unless otherwise stated. The panels in Fig. 1 show the mean fields and corresponding error estimates for *w, u,* and *v* over the global oceans that were averaged over 25 full years (1988-2012) of the analysis period (July 1987 onwards). The latitudinally banded structure in the annual-mean pattern of *w* reflects primarily the structure in the annual-mean pattern of *u*. Westerly winds exceeding 12 ms^{-1} are locations in the 30-60 degrees north and south latitudes. The trade winds of moderate wind speeds (~ 8 ms^{-1}) dictate the broad subtropical oceans, and the doldrums near the equator are under light-wind (< 5ms^{-1}) conditions all year round. On the other hand, the annual-mean pattern of *v* differs considerably from that of *u*, showing that the meridional winds associated with the Hadley circulation are most dominant over the global scale. Larges amplitude of northerlies and southerlies are all located in regions adjacent to the eastern boundary of the basin.

Despite the pattern differences in the annual-mean fields between *u* (or *w*) and *v,* the mean error patterns are surprisingly similar between the three variables, with the largest errors appearing in the same three distinct regions: the westerly belts in the northern and southern midlatitudes (40-60°) and the Intertropical Convergence Zone (ITCZ)/South Pacific Convergence Zone (SPCZ) near the equator. Errors are small in the tropical/subtropical oceans under the influence of the trade winds. The only major difference between the three sets of mean error fields is the magnitude: errors of *u* and *v* have a similar magnitude that is evidently larger than that of the *w* error. The zonally averaged plots in Fig.1 depict the variation of the errors with latitudinal bands. When averaged globally and over the 25-year period, the estimated mean error is 0.21 ms^{-1} in *w,* 0.30 ms^{-1} in *u*, and 0.32 ms^{-1} in *v.*

The monthly fields in January and July averaged over the 25-year period are shown in Figs. 2-3, respectively. Seasonal variations in *w* and *u* are characterized by the strengthening of northern (southern) hemispheric westerlies in January (July), while seasonal changes in *v* are featured by an equatorward enhancement of the southeast trades in all three tropical /subtropical basins in July. The magnitude of mean errors increases in accordance with the seasonal enhancement of prevailing winds during the respective hemisphere's winter season. For instance, large errors are located between 30-60°N in January when the Northern Hemispheric westerlies are seasonally strong, but are shifted to the latitudes between 30-60°S in July when the Southern Hemispheric westerlies are seasonally strong. Errors in the ITCZ region, particularly in the eastern tropical Pacific also become more dominant in July. The zonally averaged plots in Figs. 2-3 are a good summary of the dependence of errors on the magnitude of wind speed and components. Additionally, these plots also reveal that, consistent to what has been observed in Fig.1, the errors of the three variables all have a similar latitudinal distribution but the magnitude of errors of *u* and *v* is greater than that of *w*.

3.2 Impacts of rain and high winds

The similarity in error spatial structures between *w, u,* and *v,* despite the noted differences in the mean structure of the three variables, suggests that the errors are not controlled by the magnitude of wind speed and components. As discussed in the Introduction, rain and high winds are the two major sources of uncertainty for satellite retrieval of surface winds. The impacts of the two conditions on the uncertainty analysis are investigated here.

The OAFlux wind analysis is on a daily resolution. The rain flags from the SSMI series (SSMI F13, 16, and 17) were counted on a daily basis to form a time series of daily rain mask over the 25-year (1988-2012) period. The number of rain days per month was then constructed from the time series and the three fields shown in Figs. 4a-c represent the time-mean averages for annual mean, January, and July, respectively. Frequent rain days appear in three major latitudinal bands, including the ITCZ in the tropical oceans, the north midlatitudes (30-65°N), and the southern midlatitudes (40-65°S). The latter two latitudinal bands are known to be the regions of the mid latitude storm tracks [*Hoskins and Valdes* 1990]. On average, the number of rain days is highest in the ITCZ/SPCZ regions, with a mean of ~16 days per month over most of the Pacific sector. Seasonal changes are noted by the change of rain frequency: more rain days during the boreal summer and less in the boreal winter. The rain frequency associated with the midlatitudes storm tracks also changes with seasons, typically with enhanced activity during the hemisphere's summer season. However, the North Atlantic seems to be an exception, as there are more rain days in January than in July, particularly along the Gulf Stream and its extension.

The number of days that high winds (>15ms-1) prevail on daily basis was also counted using the same SSMI series (F13, 16, and 17). The 25-year time-mean averages for annual mean, January, and July are shown in Figs. 5a-c, respectively. Evidently, high wind events occur predominantly at higher latitudes (poleward 40° north and south) with strong coupling to the hemisphere's winter season. The occurrence of high winds is less frequent than the occurrence of rain, as there is a maximum of about only 10 days per month during the winter season.

Seasonal variations of the number of rain days and high-wind days are summarized by the zonally averaged plots in Figs. 6a-b. To evaluate their respective connection to the estimated error structures in wind speed and components, the errors of *w, u,* and *v* are also plotted using a similar format (Figs. 6c-e). One feature is clear: in the tropical oceans, the uncertainty in wind estimates is due primarily to the impacts of rain, as daily-mean winds at a high-wind category are rare (unless in tropical storm cases). Rain affects all microwave sensors. This is seen that microwave radiometers provide no retrievals in rain conditions and QuikSCAT is sensitive to heavy rain (i.e., vertically integrated rain rate greater than 2.0 km mm hr^{-1}). The removal of rain contaminated wind retrievals leads to data voids, which has to call for the background datasets (e.g. ERA interim and CFSR) to fill in missing information. The differences between reanalyzed winds and satellite winds are the cause of the uncertainty under rain conditions.

On the other hand, the extratropical regions are frequented by mid-latitude storms so that rain and high winds both contribute to error estimates. This is evidenced in the North Atlantic, where the number of rain days and high-wind days are both high in January (Figs. 4b&5b) and so errors in all components are large. A similar feature is also found in the southern Indian Ocean in July. Winter storms bring along not only powerful winds but also heavy precipitation. Under storm conditions, even without rain, the differences between sensors at high wind speeds (see Fig.10 in *Yu and Jin* [2013, JGR, submitted]) will lead to uncertainty in wind estimates. With rain in sight, the uncertainty is even greater. The reconstruction of the surface wind field associated with the storm is compounded by the fact that the mid-latitude storm is a synoptic scale low-pressure weather system featuring high temporal and spatial variability. Each satellite sensor has two passes per day, and different satellites pass at different times. The storm's surface circulation changes swiftly during the time lapse between the two passes of a sensor and between the passes of two different satellite sensors, and the situation is further complicated by the fact that none of the passes can provide a complete depiction of the storm due to the sensitivity to rain. Reanalyzed winds are the default background fields, but the differences between models and satellites under extreme conditions often do not help to alleviate the problem. Given the technical difficulties in sensors and the deficiencies of the background datasets, the uncertainty of daily wind estimates is expected to be larger in the mid-latitudes winter season than in the ITCZ regions.

3.3 Why are errors of *u* and *v* larger than errors of *w*?

Figures 7-8 illustrate one example of how the errors of *w, u*, and *v* are resulted under high winds and rain conditions. The daily field on 01 January 2005 was chosen. The rain rate retrievals averaged from the SSMI series (F13, F15, and F16) (Fig.8a) show narrow bands of rain appear mostly in the three identified latitudinal bands: the northern and southern midlatitudes in association with developing storms and the tropical oceans in association with the convective rain belts of the ITCZ and SPCZ. SSMI (Fig.8b) and QuikSCAT (Fig.7c) wind speed observations reveal vivid cyclonic circulation of the storms with accompanying high winds but there are missing values. On that day, the OAFlux daily-mean fields were constructed from seven sensors (SSMI F13, F14, F15, F16, AMSRE, WindSat wind speed, QuikSCAT). The complete fields of OAFlux *w*, *u*, and *v* are shown in Figs. 8a-c, with the corresponding error fields in Figs. 9e-g. Similarity between the three daily error fields is observed, and the pattern mirrors to a large extent the rain pattern in Fig.7a. Magnitude differences in the three error fields are observed, which are most evident in the North Pacific basin. For instance, there are four meridional bands of large *v* errors across the region between 120°E and 140°W, each of which is about 20° long. The error bands on the two sides align with the local rain bands, while the middle one, along the 180 meridian, is in a rain-free area. In fact, the contributor to this rain-free error band is the strong northerly winds (Fig. 8c). In the OAFlux analysis (Eq.(1)), input data for wind components *u* and *v* include QuikSCAT as well as ERAinterim and CFSR, while input data for wind speed *w* are satellite retrievals with atmospheric reanalyzed fields used only for filling in gaps in retrieval fields when necessary. Hence, the estimation of wind components *u* and *v* is influenced more by the background fields than the estimation of *w*. As the differences between satellite and reanalyses *u* and *v* are largest under high-wind and rain conditions, their effects on the OAFlux *u* and *v* estimates are manifested most predominantly at high northern and southern latitudes. This explains the magnitude differences in the three error components. It appears that introducing additional scatterometers is the only sensible way to improve *u* and *v* estimates, as the gaps between satellite and reanalyzed fields are too large to reconcile.

3.4 Rain and high winds detected by SSMI and QuikSCAT

Wind speed retrievals from the SSMI series rely on the measurements made at 37 GHz channels, and wind speed and vector retrievals from QuikSCAT are made at 14 GHz. Since lower frequency bands are less sensitive to rain than higher frequency bands, one can expect that SSMI wind retrievals are more sensitive to rain than QuikSCAT, and hence there are more rain flagged days in SSMI datasets. This is clearly shown in Figs. 9a-c, a comparison of the total rain amount derived from SSMI F13 with the total number of rain days derived from the respective SSMI F13 and QuikSCAT for the year 2008. SSMI provides no rain retrievals whenever rain is present. By comparison, QuikSCAT is only sensitive to heavy rain (i.e., vertically integrated rain rate greater than 2.0 km mm hr^{-1}). The difference in the sensitivity of the two sensors with regard to rain is demonstrated more clearly in the extratropical oceans, where, expect for the western boundary currents (WBCs) regimes, the amount of rain is significantly less than that in the ITCZ and SPCZ (Fig. 9a). SSMI produces more than 180 rain days for most areas poleward of 40° north and south (Fig.9b), which has at least 80 more rain days that QuikSCAT in regions away from the WBCs regimes (Fig.9c). In this sense, there are more useful wind retrievals from QuikSCAT than from one SSMI sensor – the advantage of QuikSCAT over radiometer is clearly demonstrated here, which is, QuikSCAT is a sensor not only capable of providing wind speed and direction information but also capable of providing more data coverage under similar weather conditions.

For the OAFlux synthesis, other radiometers such as AMSRE and WindSAT are also included in addition to the SSMI and the follow-on SSMIS series. Unlike the SSMI/SSMIS sensors, the AMSRE and WindSat radiometers have low frequency channels that operate at approximately 6.9 GHz and 10.8 GHz bands. *Meissner and Wentz* [2009] used WindSat to show that a combination of the low frequency channels with the V-Pol and H-Pol channels at higher frequencies allow winds to be retrieved under all rain conditions. A reduction of rain-flagged days is evident when using WindSat (not shown).

Figures 10a-b compare the number of high-wind days derived from SSMI with that from QuikSCAT in year 2008. The two patterns are remarkably similar, except that there are a few more high-wind days in SSMI than in QuikSCAT in regions such as the northern Atlantic and the southern Indian and Pacific Oceans. On an annual-mean basis, the northern Atlantic Ocean has high-wind conditions for 50-60 days. Meanwhile the northern Pacific and the southern Atlantic Ocean have less high-wind days, only about 20-30 days on average. In the southern oceans, high winds are embedded within the strong westerly wind belt and are localized at sites such as the Indian and Pacific sectors with a frequency of 50-60 days per year. It is shown in Figure 10 of *Yu and Jin* [2013, JGR, submitted] that SSMI wind retrievals are slightly higher than QuikSCAT wind retrievals in high wind conditions due presumably to the opposite effect of long wave tilting on scattering and emission when winds are strong. The high-wind frequency derived from ASMRE and WindSat (not shown) is similar to that from SSMI, indicative of the stability of high wind retrievals under rain-free conditions among the satellite radiometer products downloaded from the Remote Sensing Systems (http://www.remss.com).

The general characteristics of the dependence of *w, u,* and *v* errors on rain intensity and wind speed magnitude is examined in Fig.11a-b by using SSMI rain rate and wind speed as reference. The year 2008 was plotted. The distribution of *w, u,* and *v* errors with SSMI rain rate (Fig.11a) shows that all three errors increase steadily with rain intensity. For the rain rate in the range of 0 – 1000 cm yr^{-1}, errors of w increase from 0.2 ms^{-1} to 0.3 ms^{-1} and errors of u and v grow from 0.3 ms^{-1} up to 0.6 ms^{-1}. The u and v errors increase at a rate almost twice that of w errors as the rain rate goes up. The greater sensitivity of u and v estimates to rain intensity shown here is consistent with the analysis of Fig.6, further elucidating the impact of lack of observations under rain on the synthesis. Conversely, the distribution of errors with SSMI wind speed (Fig.11b) is more contingent to the wind speed category. At low and moderate wind speed range (2–10ms^{-1}), all three errors remain leveled at around 0.2 ms^{-1} for w and 0.3 ms^{-1} for u and v. Errors start to take off when wind speed is greater than 10ms^{-1}, and fast increase from 0.4 to 0.6 ms^{-1} when wind speed strengthens from 15 to 20 ms^{-1}. Errors of u and w show a similar rate of increase with changing wind speed, albeit the mean error of the former is higher than the latter by about 0.1ms^{-1}. Error of v, however, is more sensitive to wind conditions and has the largest rate of increase with wind speed.

3.5 Global time series of OAFlux wind analysis with error estimates

The errors discussed above refer to the STD of w, u, and v with regards to 40 sets of weight assignments. These error estimates help to address the uncertainty issues associated with the OAFlux vector wind time series. The OAFlux analysis (Eq.(1)) determines three variables, w, u, and v from 12 satellite sensors and two atmospheric reanalyses over a period of 25 years. The margin of error (denoted ME), which is used here to represent an estimate of a confidence interval for given wind estimates, can be computed from the following formula: $\mathrm{ME} = z \times \frac{\sigma_x}{\sqrt{n-1}}$, where x denotes w, u, and v, respectively, with σ_x from Eqs. 7a-c, z is the confidence coefficient, and n-1 is the degree of freedom for errors. Here n is equal to the number of input datasets used in the analysis. At the 95% confidence level, the *z* value is 1.96. Hence, the time-mean ME is 0.13 ms^{-1} for *w*, 0.19 ms^{-1} for *u*, and 0.20 ms^{-1} for *v* when averaged over the 25-year period. The annual mean time series of *w, u,* and *v* bounded by ±ME obtained for each year are shown in Figs. 12a-c.

It is evidenced from the time series that global wind speed has been strengthening during the 25-year satellite period, and the major contributor appears to be the westward intensification of zonal winds. The increase of mean zonal winds is particularly pronounced after 1997, and a rate of change at about 0.22 ms^{-1} per decade is derived over the 25-year period. The rate of change is larger than the ME estimate for *u* at the 95% confidence level and the statistical significance of the change is warranted. Interestingly, the globally averaged meridional winds remain leveled throughout the period, thus, raising important climate questions as to what and how have global zonal winds been changing in recent decades? And what drives the change?

4. Summary and discussions

A high-resolution global daily analysis of ocean-surface vector winds from 1987 onward was developed by the Objectively Analyzed air-sea Fluxes (OAFlux) project by synergizing scatterometers (wind speed and direction retrievals) and microwave passive radiometers (wind speed retrievals). This 25-year time series encompasses the entire era of satellite wind observations and shows a distinct decadal upward trend and rich variability on broad timescales [*Yu and Jin* 2012; 2013, JGR, submitted]. Yet, significance of the trend and variability can be assessed confidently only when error statistics of the time series are known. Wind retrievals have large uncertainties under rain and high winds (>15ms^{-1}), due to technical difficulties inherent to both scatterometers and radiometers. The confidence and sensitivity of the OAFlux time series to uncertainties in satellite retrievals are addressed in this study.

We found that nearly 98% of global ocean surface wind fields can be constructed with confidence from high-quality satellite wind retrievals in the low and moderate wind speed range, and the remaining 2% are affected by rain and high winds, which are currently the leading technical issues for satellite scatterometers and radiometers. Quantifying the sensitivity of the OAFlux analysis to the uncertainty in wind retrievals in rain and high wind conditions was the central focus during the development of error estimation for daily OAFlux fields of *w, u,* and *v*. The OAFlux approach is a weighted objective analysis, with the weights inversely proportional to errors in input datasets. In developing an error analysis that is specific for the OAFlux multi-sensor synthesis, we applied an ensemble-based weight-perturbed analysis to compute the statistical expectations of the cost function and to establish a statistical representation of the effects of uncertainty in satellite retrievals on the optimality of the OAFlux analysis.

A total of 40 sets of weight-based sensitivity experiments were conducted. Further increase of the number of experiments does not change the statistics, because the degree of freedom for errors is determined by the number of input datasets, not by the number of sensitivity experiments. We found that the three error fields of *w, u,* and *v* have a similar spatial pattern with large errors appearing in three distinct regions: the westerly belts in the northern and southern midlatitudes (40-60°) and the ITCZ/SPCZ rain belts in the tropical oceans. The error pattern changes with season, being more pronounced in the hemisphere's winter season when winter storms with high winds and heavy rain are the characteristics of the season. Errors are small in the tropical/subtropical oceans under the influence of the trade winds. The only difference between the three error fields is the magnitude: errors of *u* and *v* are larger than errors of *w*. When averaged globally and over the 25-year analysis period, the estimated mean STD error is 0.21 ms^{-1} in *w,* 0.30 ms^{-1} in *u*, and 0.32 ms^{-1} in *v*. Our diagnosis showed that the larger errors in *u* and *v* might be due to the sensitivity of the two components to the inclusion of the background datasets. The OAFlux synthesis determines *w, u,* and *v* from 12 sensors, but, meanwhile, also requires the use of atmospheric reanalyses as background information to fill in missing data gaps and initialize the wind direction when there are no scatterometers. Input data for wind components *u* and *v* include not only QuikSCAT and ASCAT but also ERAinterim and CFSR. By comparison, input data for wind speed *w* are scatterometers (QuikSCAT and ASCAT) and radiometers (6 SSMI sensors, 2 SSMIS sensors, AMSRE, and WindSat) with atmospheric reanalyzed fields used only for filling in data gaps when necessary. In this framework, the estimation of *u* and *v* is more dependent of the background fields than the estimation of *w*.

The margin of error (ME) at the 95% confidence level is 0.13 ms^{-1} for *w*, 0.19 ms^{-1} for *u*, and 0.20 ms^{-1} for *v*, when averaged over the 25-year period. The OAFlux time series show that global wind speed has been strengthening during the 25-year satellite period, characterized by westward intensification of global zonal winds, particularly pronounced after 1997. A rate of change at about 0.22 ms^{-1} per decade is derived over the 25-year period, which is statistically significant at the 95% confidence level given the estimate of ME of *u*.

Our study showed that the sensitivity of the OAFlux multi-sensor synthesis to the uncertainty in wind retrievals under rain and high wind could be quantified by using an ensemble-based posteriori diagnostics. It appears that the likelihood for further reducing the uncertainty of a multi-sensor synthesis is when multiple scatterometers are available to provide sufficient global coverage and to minimize the need of reanalyses as the background datasets. Currently, the satellite ocean-wind observing system reaches a historical three-scatterometer constellation that features ASCAT aboard EUMESAT MetOP-A and -B, and the Indian OceanSat-2 scatterometer launched by ISRO. ASCAT-A and –B are less sensitive to rain and OceanSat-2 has a global daily coverage equivalent to QuikSCAT. The three when combined present a unique opportunity to improve the understanding and estimation of the wind estimates under all weather conditions.

Acknowledgements

The project is sponsored by the NASA Ocean Vector Wind Science Team (OVWST) activities under grant NNA10AO86G. We thank the support and technical inputs from the international OVWST members during the five-year development of the OAFlux wind synthesis products. The satellite wind products of SSMI, SSMIS AMSRE, and QuikSCAT were downloaded from Remote Sensing Systems at http://www.ssmi.com/, and ASCAT datasets from NASA JPL PO.DAAC at http://podaac.jpl.nasa.gov. The original ASCAT datasets are hosted by KNMI at http://www.knmi.nl/scatterometer. The ERA-interim winds were from NCAR Research Data Archive at http://dss.ucar.edu and the original datasets are produced by ECMWF. CFSR winds were obtained from NCEP/CFSR data archives at NCDC NOMADS data access.

References

Adler, R. F., G. Gu, and G. J. Huffman (2012). Estimating Climatological Bias Errors for the Global Precipitation Climatology Project (GPCP). *J. Appl. Meteor. Climatol.*, **51**, 84–99. doi: http://dx.doi.org/10.1175/JAMC-D-11-052.1

Atlas, R., R. N. Hoffman, J. Ardizzone, S. M. Leidner, J. C. Jusem, D. K. Smith, and D. Gombos (2011). A cross-calibrated, multiplatform ocean surface wind velocity product for meteorological and oceanographic applications. *Bull. Amer. Meteor. Soc.*, **92**, 157–174. doi: 10.1175/2010BAMS2946.1.

Bentamy , A., S. A. Grodsky, J. A. Carton, D. Croizé-Fillon, and B. Chapron, (2012). Matching ASCAT and QuikSCAT winds. *J. Geophys. Res.,* **117**, C02011, doi:10.1029/2011JC007479.

Bourassa, M. A., and K. M. Ford, (2010). Uncertainty in Scatterometer-Derived Vorticity. *J. Atmos. Oceanic Technol.*, **27**, 594–603. doi: http://dx.doi.org/10.1175/2009JTECHO689.1

Daley, R. (1991). *Atmospheric Data Analysis.* Cambridge University Press. 457pp.

Desroziers, G., L. Berre, V. Chabot, and B. Chapnik (2009). A Posteriori Diagnostics in an Ensemble of Perturbed Analyses. *Mon. Wea. Rev.*, **137**, 3420–3436. doi: http://dx.doi.org/10.1175/2009MWR2778.1

Donelan, M.A., and W. J. Pierson, Jr. (1987). Radar scattering and equilibrium ranges in wind-generated waves with application to scatterometry. *J. Geophys. Res.,* **92**, 4971-5030.

Dunbar, R. S., (1998). *NASA scatterometer science data product (NSCAT-2) User's Manual - overview and geophysical data products*. JPL Document, D-12985 Manual Version 1.2, February 1998.

Dunbar, R., and Coauthors, (2006). *QuikSCAT science data product user manual*, version 3.0. JPL

Doc. D-18053—Rev. A, Jet Propulsion Laboratory, Pasadena, CA, 85 pp.

Fangohr, S., and E. C. Kent, (2012). An estimate of structural uncertainty in QuikSCAT wind vector retrievals. *J. Appl. Meteor. Climatol.,* **51**, 954–961.

Freilich, M. H., (1997). Validation of vector magnitude datasets: Effects of random component errors. *J. Atmos. Oceanic Technol*., **14**, 695–703.

Freilich, M. H., and B. A. Vanhoff, (2003). The relationship between winds, surface roughness, and radar backscatter at low incidence angles from TRMM precipitation radar measurements. *J. Atmos. Oceanic Technol*., **20**, 549–562.

Grantham, W., E. M. Bracalente, W. L. Jones, and J. W. Johnson, (1977). The SeaSat-A satellite scatterometer. *IEEE J. Oceanic Engineering*, **2**(2), 200-206, doi: 10.1109/JOE.1977.1145338.

Hoffman, R. N. (1984). SASS wind ambiguity removal by direct minimization. Part II: Use of smoothness and dynamical constraints. *Mon. Wea. Rev.*, **112**, 1829–1852.

Hoffmann, R. N., S. M. Leidner, J. M. Henderson, R. Atlas, J. V. Ardizzone, and S. C. Bloom, (2003). A two-dimensional variational analysis method for NSCAT ambiguity removal: Methodology, sensitivity, and tuning. *J. Atmos. Oceanic Technol.*, **20,** 585–605.

Hoskins, B. J., and P. J. Valdes, (1990). On the existence of storm-tracks. *J. Atmos. Sci.*, **47**, 1854–1864. doi: http://dx.doi.org/10.1175/1520-0469(1990)047<1854:OTEOST>2.0.CO;2.

Kent, E. C., and P. G. Challenor (2006).Toward estimating climatic trends in SST. Part II: random errors. *J. Atmos. Oceanic Technol.*, **23**(3). 476-486. 10.1175/JTECH1844.1.

Kent, E.C., and A. Kaplan (2006). Toward estimating climatic trends in SST. Part III: systematic biases. *J. Atmos. Oceanic Technol.,* **23**(3). 487-500. 10.1175/JTECH1845.1.

Legler, D. M., I. M. Navon, and J. J. O'Brien, (1989). Objective Analysis of pseudo-stress over the Indian Ocean using a direct minimization approach. *Mon. Wea. Rev*., **117**, 709-720.

Lorenc, A. C., (1988). Optimal nonlinear Objective Analysis. *Quart. J. Roy. Met. Soc*., **114**, 205-240.

Meissner, T., and F. J. Wentz, (2009). Wind vector retrievals under rain with passive satellite microwave radiometers. *IEEE Trans. Geosci. Remote Sens.*, **47**(9), 3065-3083.

Milliff, R. F., J. Morzel, D. B. Chelton, and M. H. Freilich, (2004). Wind Stress Curl and Wind Stress Divergence Biases from Rain Effects on QSCAT Surface Wind Retrievals. *J. Atmos. Oceanic Technol.*, **21**, 1216–1231. doi: http://dx.doi.org/10.1175/1520-0426(2004)021<1216:WSCAWS>2.0.CO;2.

Plant, W.J., D.E. Weissman, W.C. Keller, V. Hesany, K. Hayes, and K.W. Hoppel (1999). Air/sea momentum transfer and the microwave cross section of the sea. *J. Geophys. Res,* **101**, 11,173-11,192.

Portabella, M., and A. Stoffelen, (2001). Rain Detection and Quality Control of SeaWinds. *J. Atm. Oceanic Technol.*, **18**, 7, 1171-1183.

Portabella, M., A. Stoffelen, W. Lin, A. Turiel, A. Verhoef, J. Verspeek, and J. Ballabrera-Poy (2012). Rain effects on ASCAT-retrieved winds: toward an improved quality control. *IEEE Trans. Geosci. Remote Sens.*, **50**(7), 2495-2506.

Quilfen, Y., B. Chapron, T. Elfouhaily, K. Katsaros, and J. Tournadre, (1998). Observation of Tropical Cyclones by High-Resolution Scatterometry. *J. Geophys. Res.,* **103**(C4), 7767-7786.

Reynolds, R. W., T. M. Smith, C. Liu, D. B. Chelton, K. S. Casey, and M. G. Schlax, (2007). Daily High-Resolution-Blended Analyses for Sea Surface Temperature. *J. Climate*, **20**, 5473–5496. doi: http://dx.doi.org/10.1175/2007JCLI1824.1

Ricciardulli, L, and F. J. Wentz, (2011). Reprocessed QuikSCAT (V04) Wind Vectors With Ku-2011 Geophysical Model Function, Report # 043011, Remote Sensing Systems, Santa Rosa, CA, 8 pp.

Schlax, M. G., D. B. Chelton, and M. H. Freilich, (2001). Sampling errors in wind fields constructed from single and tandem scatterometer datasets. *J. Atmos. Oceanic Technol.*, **18,** 1014–1036.

Smith, T. M., and R. W. Reynolds, (2004). Improved Extended Reconstruction of SST (1854–1997). *J. Climate*, **17**, 2466–2477. doi: http://dx.doi.org/10.1175/1520-0442(2004)017<2466:IEROS>2.0.CO;2.

Soisuvarn, S., Z. Jelenak, P. S. Chang, Q. Zhu, and G. Sindic-Rancic, (2008). Validation of NOAA's near real-time ASCAT ocean vector winds. *Proc. IGARSS*, I118–121.

Stiles, B., and S. Yueh, (2002). Impact of rain on wind scatterometer data. *IEEE Trans. Geosci. Remote Sensing*., **40**, 1973–1983.

Stoffelen, A., (1998). Toward the true near-surface wind speed: Error modeling and calibration using triple collocation. *J. Geophys. Res.*, **103,** 7755–7766.

Stoffelen, A., and D. Anderson, (1997). Scatterometer data interpretation: Estimation and validation of the transfer function CMOD4. *J. Geophys. Res.,* **102**, 5767–5780.

Talagrand, O., (1997). Assimilation of observations, an introduction. *J. Met. Soc. Japan*, **75**, 191–209.

Vogelzang, J., A. Stoffelen, A. Verhoef, and J. Figa-Saldaña (2011).On the quality of high-resolution scatterometer winds. *J. Geophys. Res.*, **116**, C10033, doi:10.1029/2010JC006640.

Weissman, D. E., W. J. Plant, W. C. Keller, and V. G. Irisov, (2002a). Comparison of scatterometer and radiometer wind vector measurements. *J. Atmos. Oceanic Technol.,* **19**, 100–113.

Weissman, D., M. A. Bourassa, and J. Tongue, (2002b). Effects of rain rate and magnitude on SeaWinds scatterometer wind speed errors. *J. Atmos. Oceanic Technol*., 19, 738–746.

Weissman, D. E., B. W. Stiles, S. M. Hristova-Veleva, D. G. Long, D. K. Smith, K. A. Hilburn, and W. L. Jones, (2012). Challenges to Satellite Sensors of Ocean Winds: Addressing Precipitation Effects. *J. Atmos. Oceanic Technol.*, **29**, 356–374. doi: http://dx.doi.org/10.1175/JTECH-D-11-00054.1.

Wentz, F., (1997). A well-calibrated ocean algorithm for SSM/I. *J. Geophys. Res.*, **102**, 8703-8718.

Wentz, F. J., T. Meissner, and D. Smith, (2005). Evaluation of microwave scatterometers and radiometers as satellite anemometers. Geoscience and Remote Sensing Symposium, IGARSS '05. Proceedings. 2005 IEEE International, **5**, 3310 - 3313, July 2005.

Yu, L., and X. Jin, (2012). Buoy perspective of a high-resolution global ocean vector wind analysis constructed from passive radiometers and active scatterometers (1987-present). *J. Geophys. Res*., **117**, C11013, doi:10.1029/2012JC008069.

Yu, L., and X. Jin, (2013a), A Satellite-Derived High-Resolution Ocean Surface Vector Wind Analysis (1987 onwards). Part I: Insights on the synergy between multiple sensors. Submitted.

Yu, L., and X. Jin (2013b). A satellite-derived high-resolution ocean surface vector wind analysis (1987 onwards). Part II. Confidence and sensitivity to rain and high winds. Submitted.

Yueh, S., W. J. Wilson, F. K. Li, S. V. Nghiem, and W. B. Ricketts, (1997), Polarimetric brightness temperatures of sea surfaces measured with aircraft K- and Ka-band radiometers. *IEEE Trans. Geosci. Remote Sens*., **35**, 1177–1187.

Yueh, S. H., B. W. Stiles, W.-Y. Tsai, H. Hu, and W. T. Liu, (2001), QuikSCAT geophysical model function for tropical cyclones and applications to Hurricane Floyd. *IEEE Trans. Geosci. Remote Sensing*, **39**, 2601–2612.

Figure Captions

Figure 1. The 25-year time-mean of the OAFlux wind fields and uncertainty estimates. Left column: the annual mean fields of (a) wind speed, (b) zonal (positive eastward), and (c) meridional (positive northward) winds. Center column: the annual mean error fields of (d) wind speed, (e) zonal and (f) meridional winds. Right column: zonally averaged annual-mean values for (g) wind speed and associated error estimates, (h) zonal wind and associated error estimates, and (i) meridional wind and associated error estimates.

Figure 2. Same as Figure 1 but for time-mean January.

Figure 3. Same as Figure 1 but for time-mean July.

Figure 4. Averaged number of rain days per month constructed from SSMI/SSMIS sensors (F13, F16, and F17) during the 1988-2012 period. (a) Annual mean, (b) January, and (c) July. Unit: number of days per month.

Figure 5. Averaged number of high-wind ($>15 ms^{-1}$) days per month constructed from SSMI/SSMIS sensors (F13, F16, and F17) during the 1988-2012 period. (a) Annual mean, (b) January, and (c) July. Unit: number of days per month.

Figure 6. Zonally averaged values for annual mean (thick black), January (blue), and July (red) over the 25-year period (1988-2012). (a) Rain days per month, (b) High wind days per month, (c) estimated error of wind speed, (d) estimated error of zonal wind, and (e) estimated error of meridional wind.

Figure 7. Case study of daily-mean fields from satellite observations on 01 January 2005. (a) rain rate from SSMI F13, (b) wind speed from SSMI F13, and (c) wind speed from QuikSCAT.

Figure 8. Case study of the OAFlux daily-mean winds and associated error estimates on 01 January 2005. (a) wind speed, (b) zonal wind, (c) meridional wind, (d) estimated error of wind speed, (e) estimated error of zonal wind, and (f) estimated error of meridional wind.

Figure 9. (a) Annual-mean averaged rain rate in 2008 derived form SSMI F13, (b) the total number of rain days in 2008 constructed from SSMI F13, and (c) the total number of rain days in 2008 from QuikSCAT.

Figure 10. The total number of high-wind days in 2008 constructed from (a) SSMI F13 and (b) QuikSCAT.

Figure 11. Increase of the error of wind speed with (a) SSMI F13 rain rate and (b) SSMI F13 wind speed constructed from daily-mean fields in 2008.

Figure 12. OAFlux annual-mean time series (thick black line) of (a) wind speed, (b) zonal wind, and (c) meridional wind during 1988-2012 bounded by ± ME (margin of error; gray shaded areas) for the respective component at the 95% confidence level.

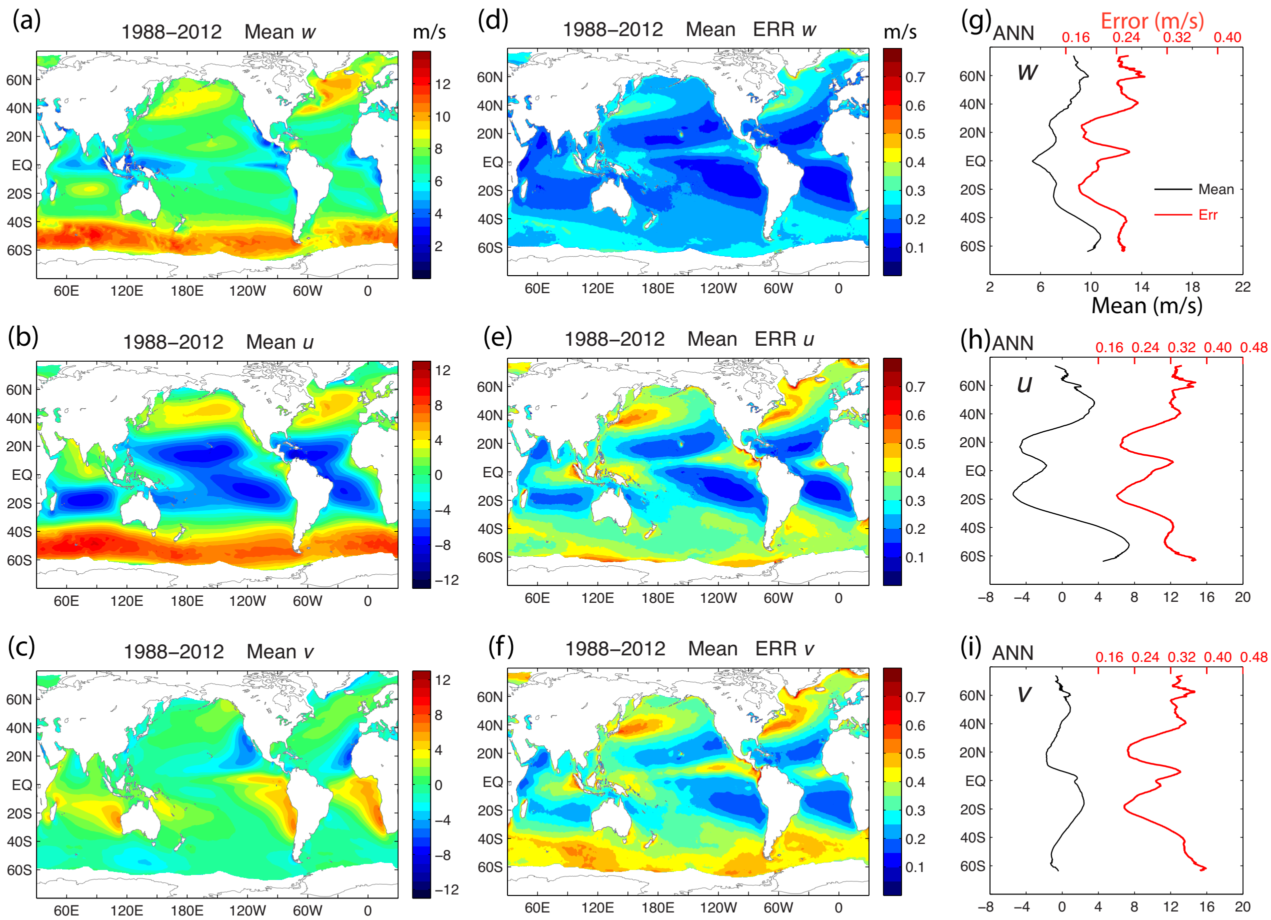

Figure 1. The 25-year time-mean of the OAFlux wind fields and uncertainty estimates. Left column: the annual mean fields of (a) wind speed, (b) zonal (positive eastward), and (c) meridional (positive northward) winds. Center column: the annual mean error fields of (d) wind speed, (e) zonal and (f) meridional winds. Right column: zonally averaged annual-mean values for (g) wind speed and associated error estimates, (h) zonal wind and associated error estimates, and (i) meridional wind and associated error estimates.

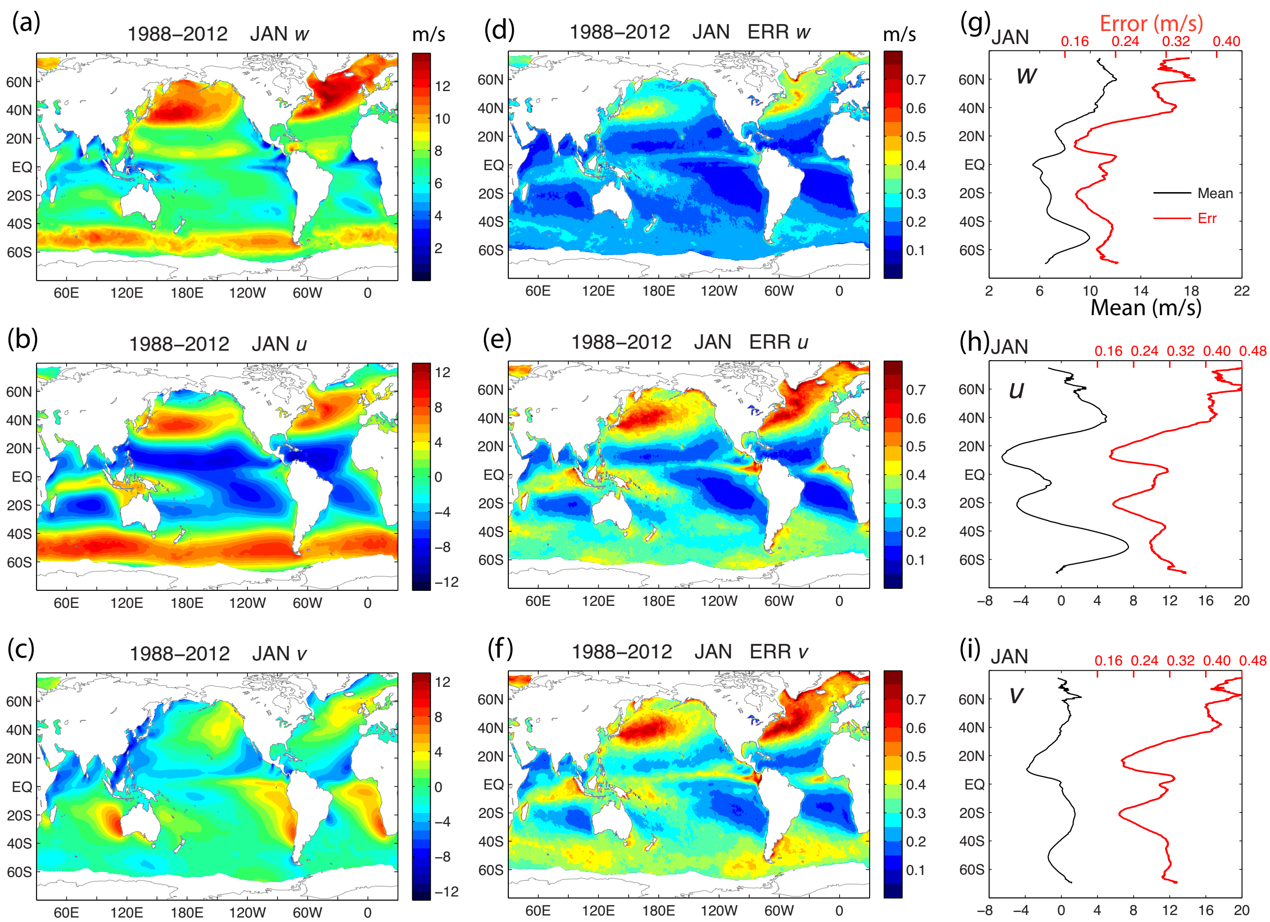

Figure 2. Same as Figure 1 but for time-mean January.

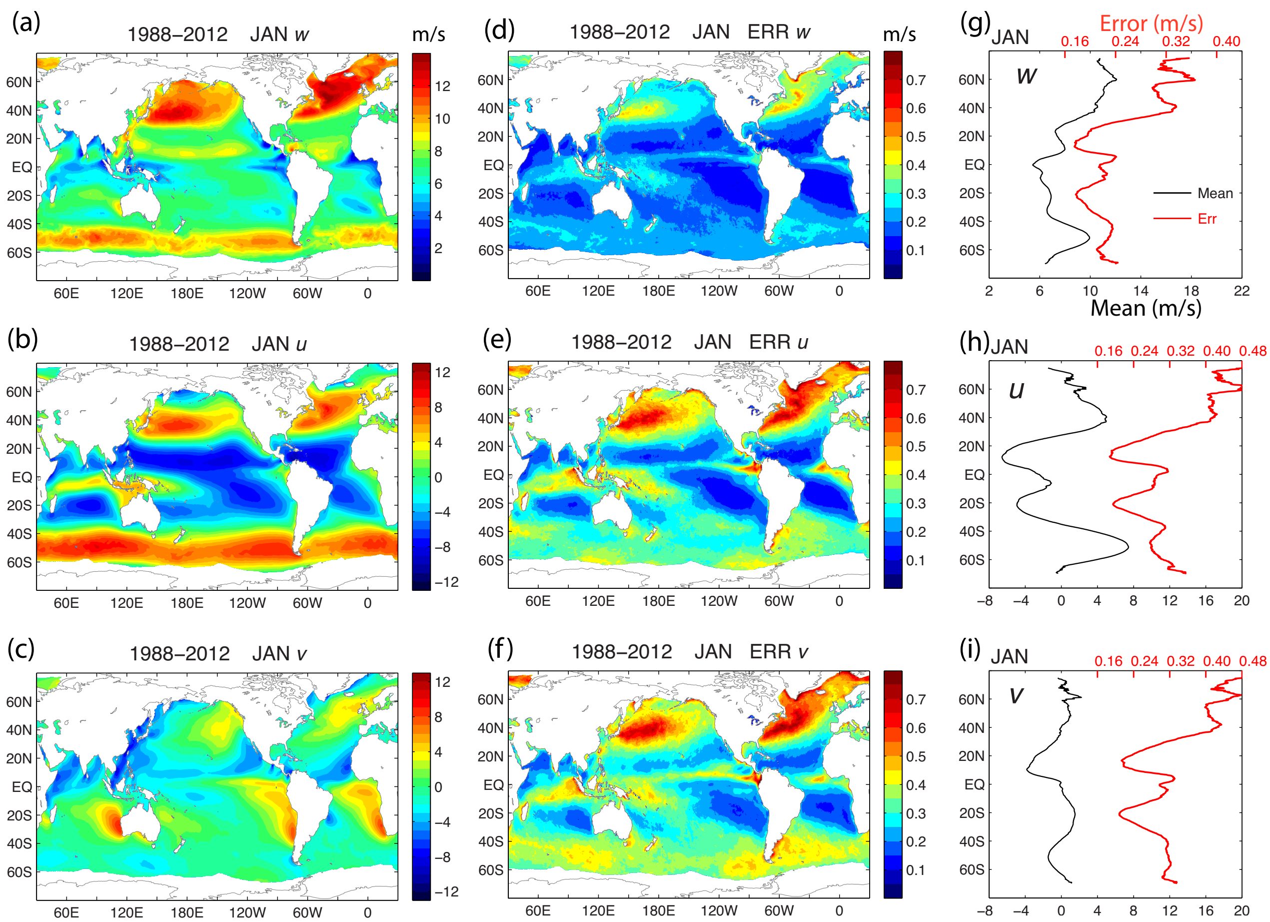

Figure 3. Same as Figure 1 but for time-mean July.

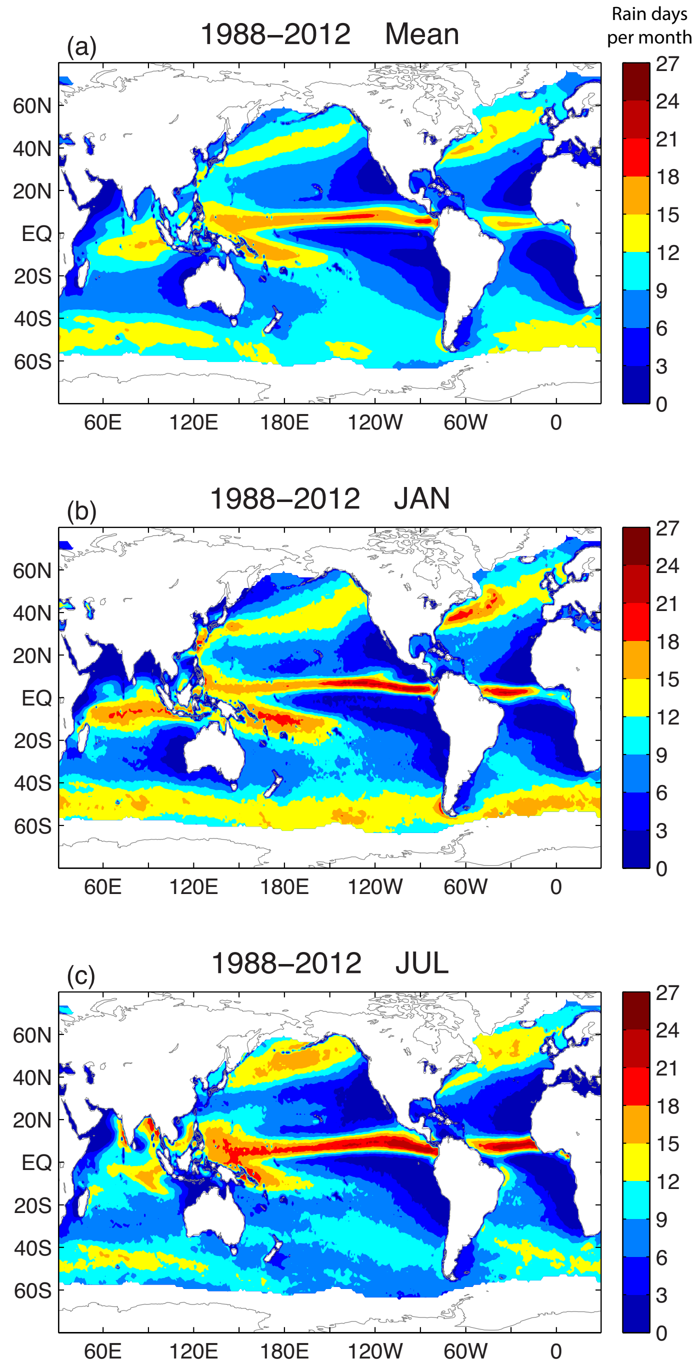

Figure 4. Averaged number of rain days per month constructed from SSMI/SSMIS sensors (F13, F16, and F17) during the 1988-2012 period. (a) Annual mean, (b) January, and (c) July. Unit: number of days per month.

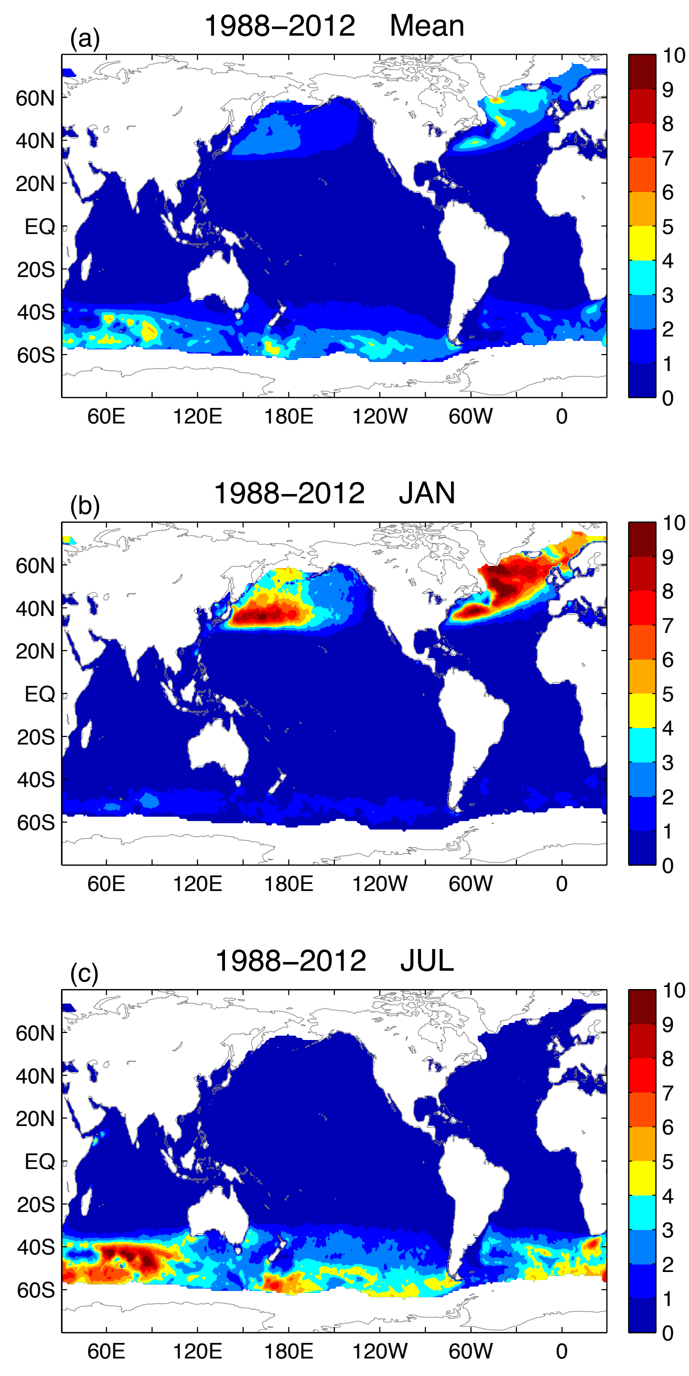

Figure 5. Averaged number of high-wind (>15ms^{-1}) days per month constructed from SSMI/SSMIS sensors (F13, F16, and F17) during the 1988-2012 period. (a) Annual mean, (b) January, and (c) July. Unit: number of days per month.

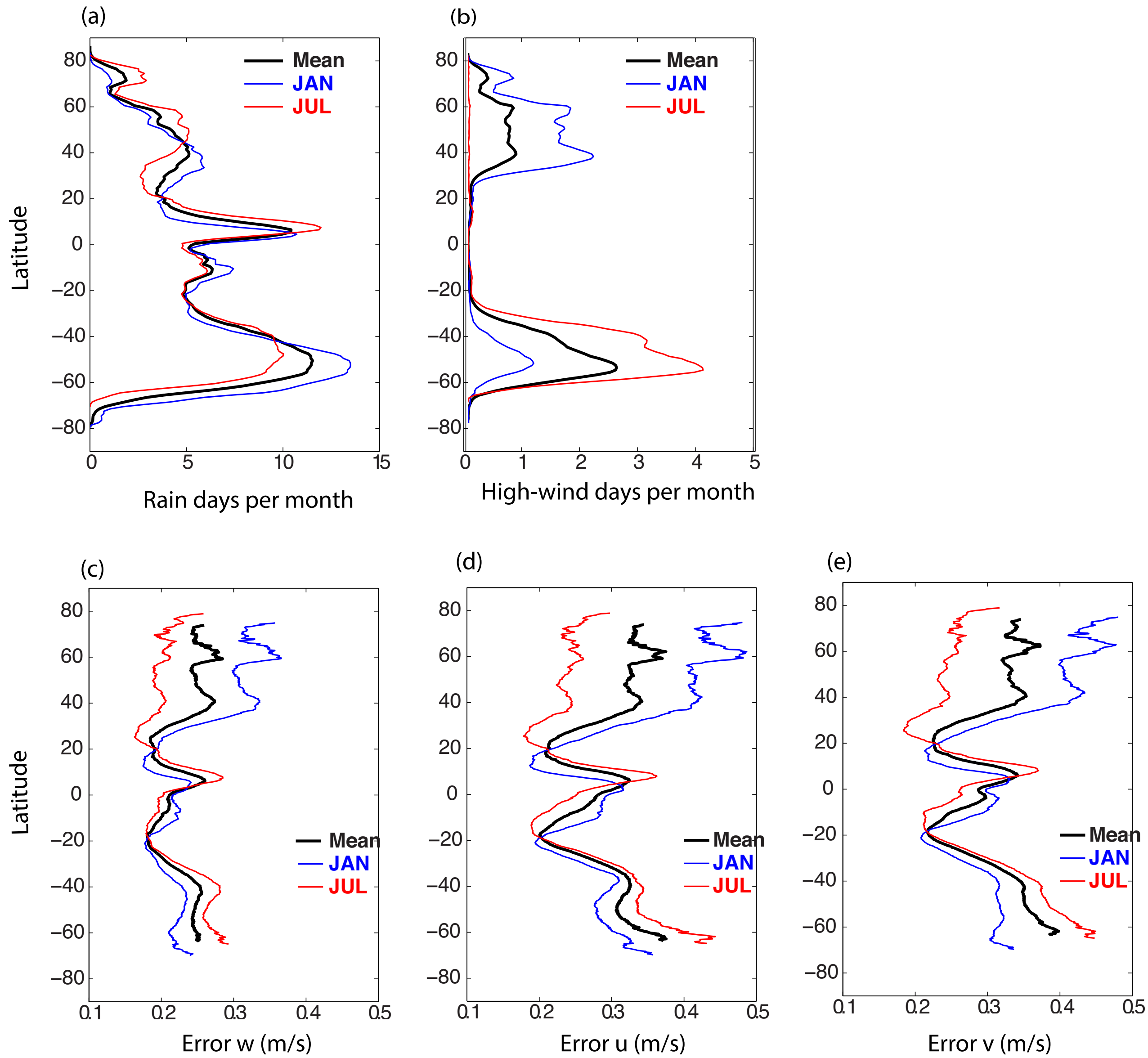

Figure 6. Zonally averaged values for annual mean (thick black), January (blue), and July (red) over the 25-year period (1988-2012). (a) Rain days per month, (b) High wind days per month, (c) estimated error of wind speed, (d) estimated error of zonal wind, and (e) estimated error of meridional wind.

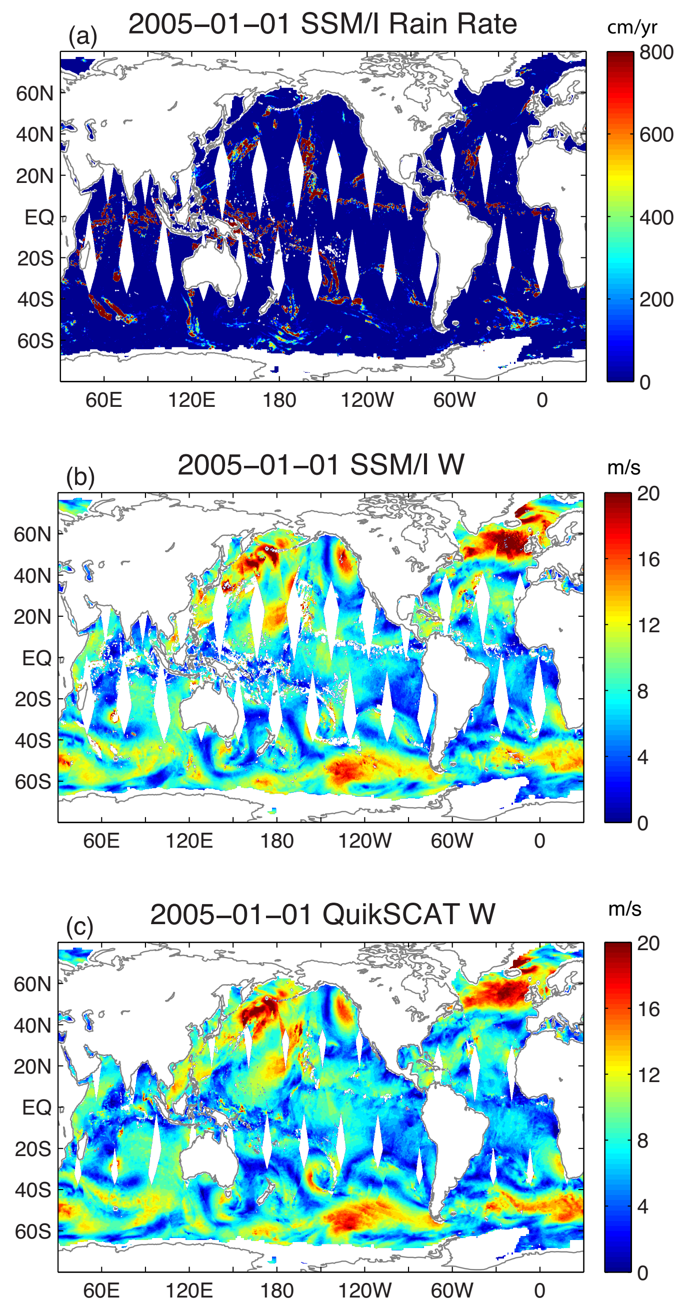

Figure 7. Case study of daily-mean fields from satellite observations on 01 January 2005. (a) rain rate from SSMI F13, (b) wind speed from SSMI F13, and (c) wind speed from QuikSCAT.

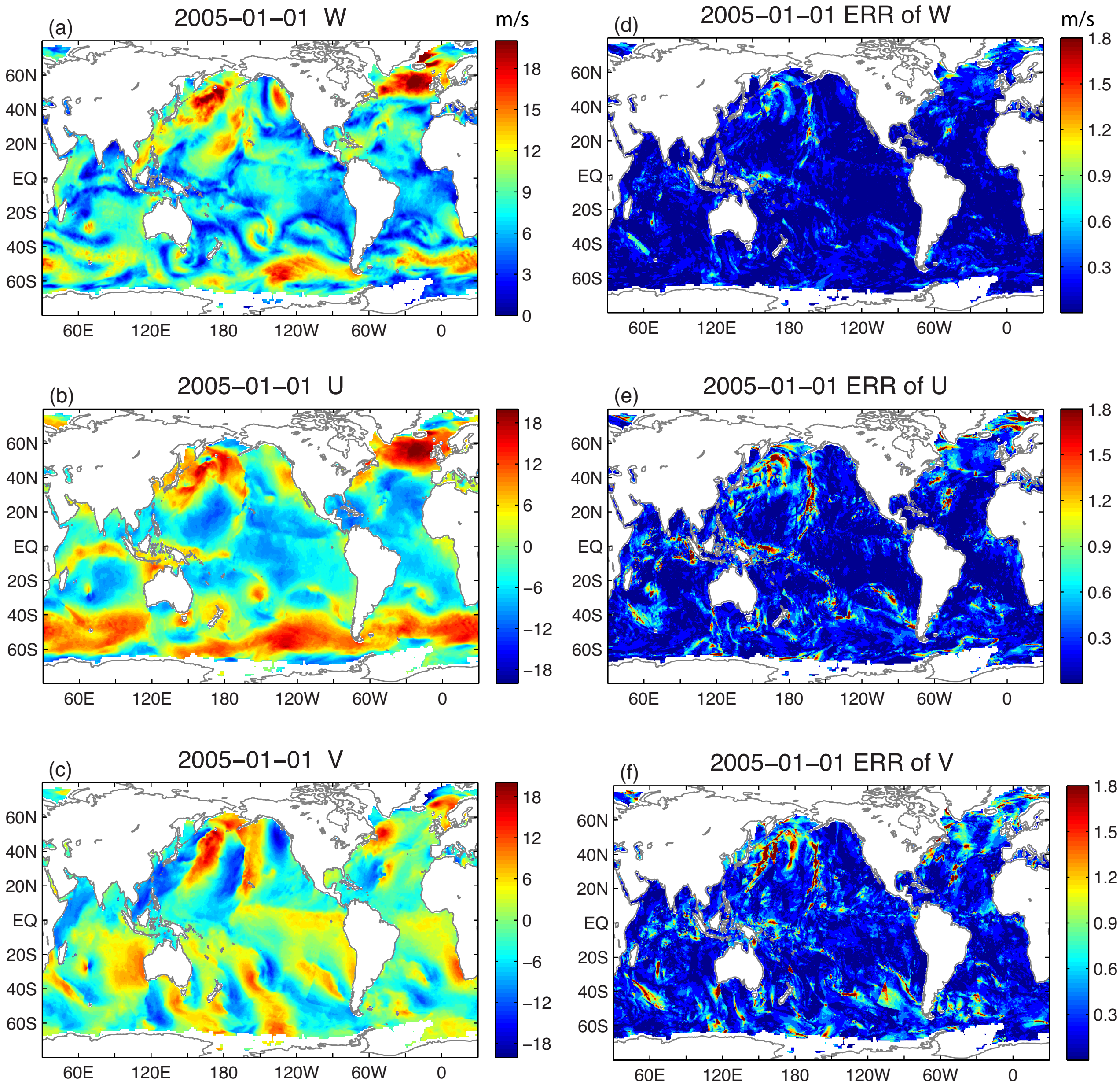

Figure 8. Case study of the OAFlux daily-mean winds and associated error estimates on 01 January 2005. (a) wind speed, (b) zonal wind, (c) meridional wind, (d) estimated error of wind speed, (e) estimated error of zonal wind, and (f) estimated error of meridional wind.

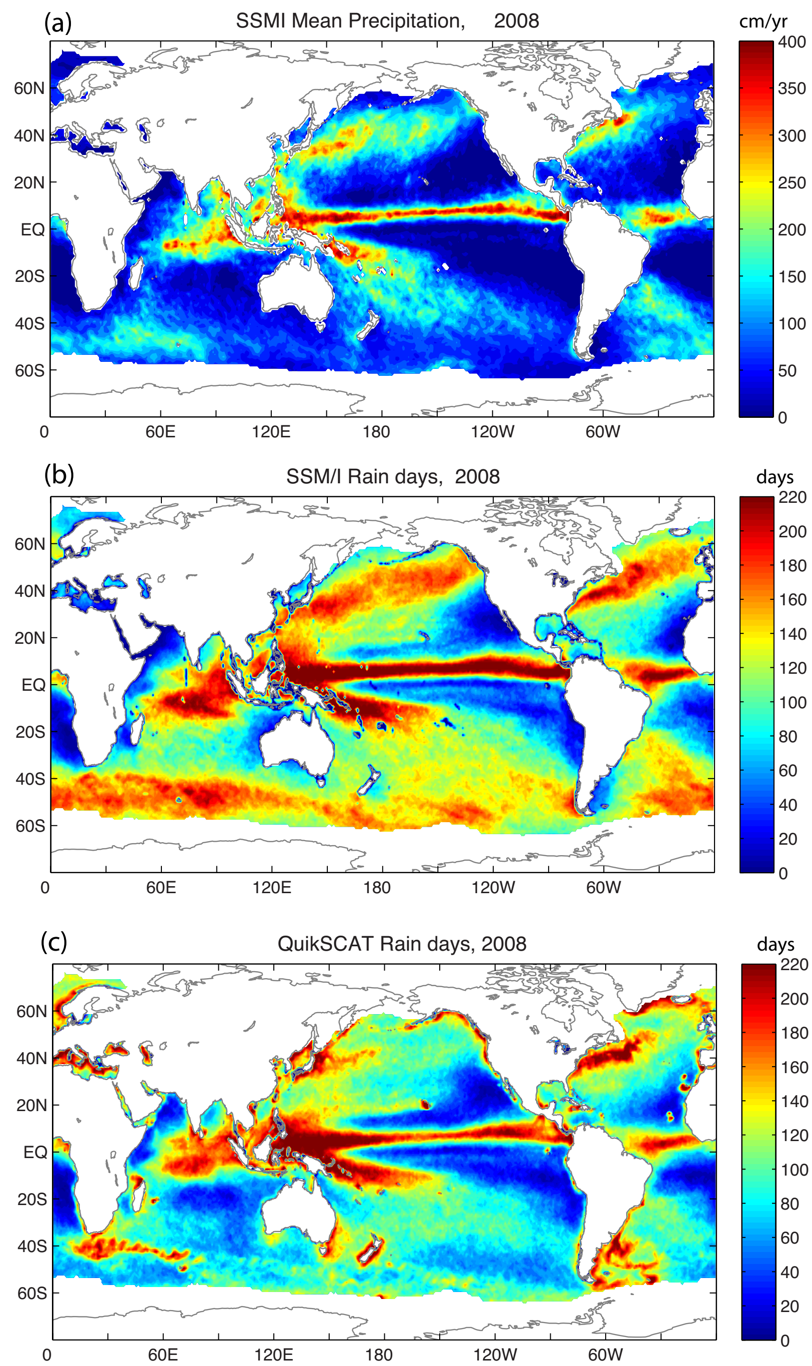

Figure 9. (a) Annual-mean averaged rain rate in 2008 derived form SSMI F13, (b) the total number of rain days in 2008 constructed from SSMI F13, and (c) the total number of rain days in 2008 from QuikSCAT.

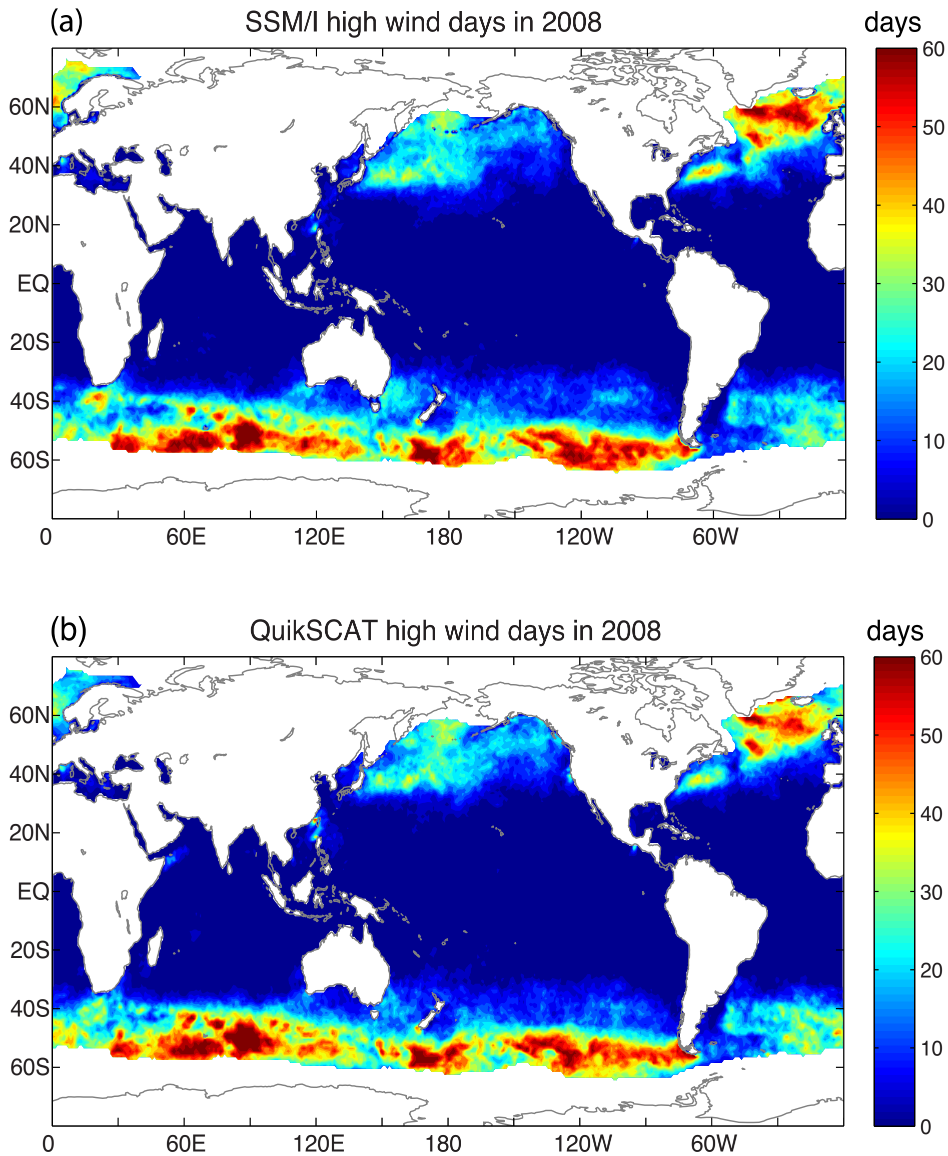

Figure 10. The total number of high-wind days in 2008 constructed from (a) SSMI F13 and (b) QuikSCAT.

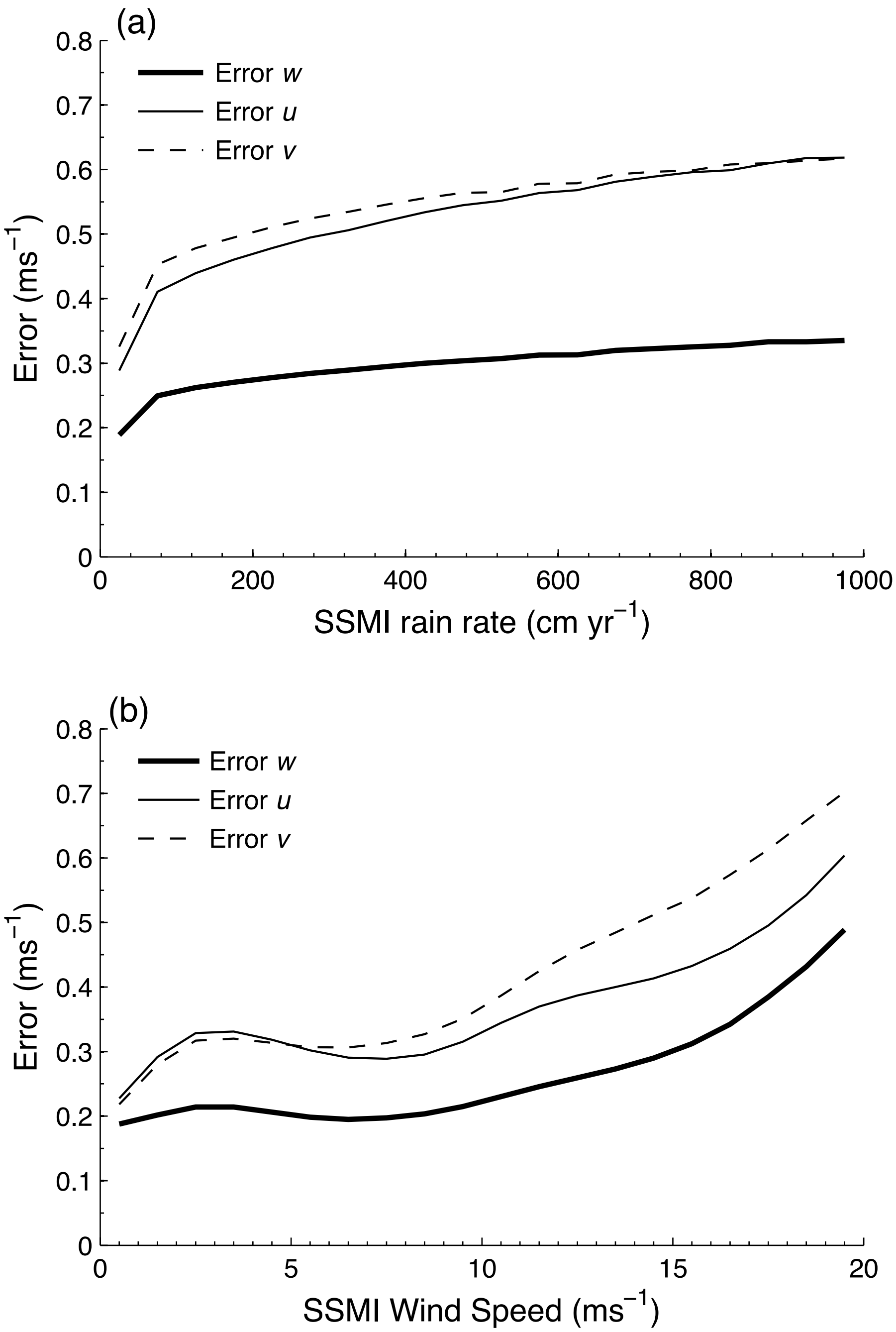

Figure 11. Increase of the error of wind speed with (a) SSMI F13 rain rate and (b) SSMI F13 wind speed constructed from daily-mean fields in 2008.

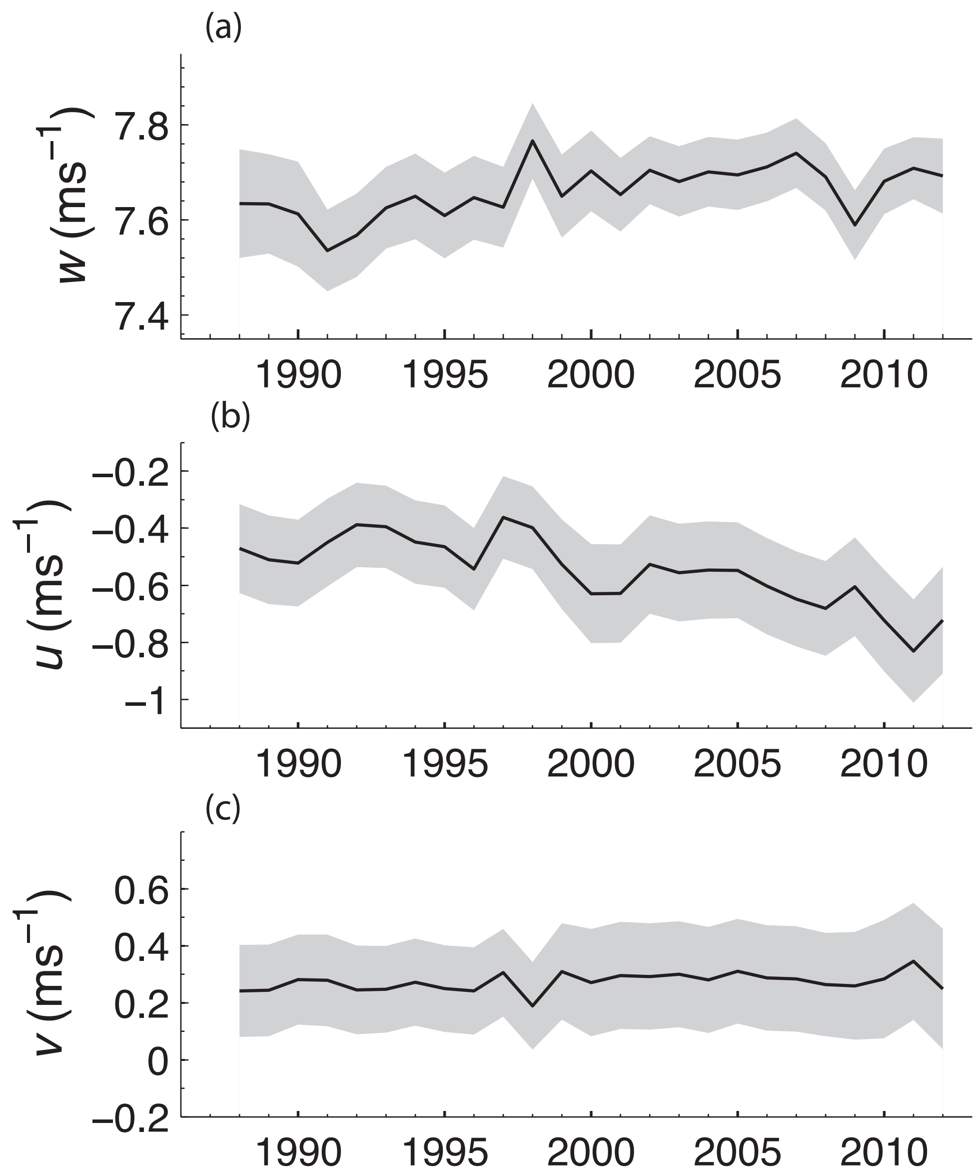

Figure 12. OAFlux annual-mean time series (thick black line) of (a) wind speed, (b) zonal wind, and (c) meridional wind during 1988-2012 bounded by ± ME (margin of error; gray shaded areas) for the respective component at the 95% confidence level.